Atmos. Chem. Phys. Discuss., 12, 20351–20382, 2012
www.atmos-chem-phys-discuss.net/12/20351/2012/
doi:10.5194/acpd-12-20351-2012

Atmospheric Chemistry and Physics Discussions

Preliminary signs of the initiation of deep convection by GNSS

H. Brenot[1], J. Neméghaire[2], L. Delobbe[2], N. Clerbaux[2], and M. Van Roozendael[1]

[1]Belgian Institute for Space Aeronomy, Avenue Circulaire 3, 1180 Brussels, Belgium
[2]Royal Meteorological Institute of Belgium, Avenue Circulaire 3, 1180 Brussels, Belgium

Received: 4 July 2012 – Accepted: 19 July 2012 – Published: 14 August 2012

Correspondence to: H. Brenot (brenot@oma.be)

Published by Copernicus Publications on behalf of the European Geosciences Union.

Abstract

This study reports on the exploitation of GNSS for weather forecasts, especially for nowcasting. We focus on GPS observations (post-processing with a time resolution of 15 min) and try to establish typical configurations of the humidity field which characterise convective systems and particularly which supply forerunners of their initiation associated with deep convection. We show the critical role of GNSS horizontal gradients of humidity to detect small scale structures of the troposphere (i.e. convective cells), and then we present our strategy to obtain typical water vapour configurations by GNSS, called "H_2O alert". These alerts are based on a dry/wet contrast taking place during a 30 min window before initiation of a convective system. GNSS observations have been assessed for the rainfall event of the 28–29 June 2005 using data from the Belgian dense network (baseline from 5 to 30 km). To validate our GNSS H_2O alert, we use the detection of precipitation by C-band weather radar and thermal infrared radiance of the 10.8-µm channel [Ch09] of SEVIRI instrument on METEOSAT Second Generation. Our H_2O alert obtains a score of about 80 %.

1 Introduction

For 20 yr, data from ground-based GNSS (Global Navigation Satellite System) receivers have been used to accurately measure the path delay of the neutral atmosphere which highly depends on the water vapour content above the associated antenna (Bevis et al., 1992). The mean meteorological observation is generally called zenith path delay or Zenith Total Delay (ZTD) of the neutral atmosphere. This observation (1st order), which describes the mean delay above a GNSS site, can also be associated with a 2nd order observation of the neutral atmosphere: the horizontal gradient of delay $\vec{G}$ (North-South and East-West components) (Chen and Herring, 1997).

The objective of this work is to show the value of GNSS observations for weather forecasts, especially for nowcasting. We will focus on GPS observations of ZTD and

ACPD
12, 20351–20382, 2012

$\vec{G}$ (post-processing with a time resolution of 15 min) and try to answer to the following question:

"Can the detection of water vapour by GNSS allow us to establish typical configurations of the humidity field which characterise convective systems and particularly which supply forerunners of their initiation associated with deep convection?"

After a brief presentation of the rainfall event of the 28–29 June 2005 (case study of this paper), we will show the value of horizontal GNSS gradients of delay to detect small scale structures in the troposphere (Davis et al., 1993; Chen and Herring, 1997; Gradinarsky, 2002). An improvement of the humidity field observed by GNSS considering gradients will be shown. Then, using a new detection of humidity structures, we will present our strategy to obtain a GNSS indicator of the initiation of deep convection. To validate our typical configurations of the humidity field (based on a dry/wet contrast obtained by GNSS), called "H_2O alert", we will use two other indicators of deep convection obtained by meteorological radar and SEVIRI instruments on METEOSAT Second Generation. We will present these two indicators (detection of precipitation by C-band weather radar and thermal infrared radiance of the 10.8-µm channel [Ch09] by SEVIRI instrument) and show statistical results of our H_2O alerts for the 28–29 June 2005 rainfall event. Then we will highlight some conditions and perspectives in order to show how our GNSS H_2O alerts can be used an operational nowcasting system.

2 Rainfall event of the 28–29 June 2005

From the afternoon of the 28 to the evening of the 29 June 2005, a continuous period of precipitation was observed over the main part of Belgium (see Fig. 1). Between 10:00 and 16:00 UTC on the 29 June, surface analysis indicated a convective episode over Belgium. Using the Belgian synoptic network (pressure and surface winds), lines of convergences have been identified during this event. These are associated with a low pressure trough as shown at 12:00 UTC (29 June 2010) Fig. 2.

ACPD
12, 20351–20382, 2012

Lines of convergence took place in hot and very wet air which had invaded Belgium during the night (28–29 June 2005). In a few hours in the neighbourhood of these lines, several clusters of convective cells were developing (see hourly radar precipitation Fig. 1).

A dynamic coupling between a marked trough centred on North-Western France and a complex surface depression over Belgium had reinforced air instability. Several convective cells were observed by the SEVIRI instrument on METEOSAT (InfraRed channel). Thick cumuli form clouds with high vertical extensions and cold tops were associated with these cells (see Fig. 3). At the beginning, clusters were distinct with a spatial extension of about 10 km. But finally clusters were stretched by high altitude air currents (associated with a depression coming from France) and by the impact of the vertical shear of the wind. The intensification of convective activity induced a complex meso-scale convective system. Gradually this system covered the major part of Belgium resulting in downpours and thunderstorms. In the north-west of the country, the convective activity was limited (see Fig. 1). Neméghaire and Brenot (2010) give a precise description of this meteorological event.

The forecast of rainfall from this complex convective system, using the ALADIN numerical weather prediction model, data from the Belgian synoptic network and the near-real time meteorological observations (radar, SAFIR, METEOSAT), was not a success.

3 GNSS Humidity field with geodetic software

3.1 Precise positions and neutrosphere measurements

Since 1992 (Bevis et al., 1992), GNSS has been used to characterise the humidity field. We have measured ZTD and horizontal gradients of delay with the GAMIT geodetic software (version 10.4, Herring et al., 2010). To measure such atmospheric observations, a precise knowledge of the positions of all GNSS stations is required. For this reason, a primary analysis has been processed to estimate precise coordinates for all

ACPD
12, 20351–20382, 2012

the local stations (about 70) of the Belgian dense network. Sessions with 24 h of measurements for a period of 5 days have been considered (tropospheric delays estimated every 2 h). An unconstrained daily GAMIT positioning solution has been obtained and converted into a final global solution in the ITRF2000 reference frame (Altamimi et al., 2002) where GLOBK Kalman filter (Herring et al., 1990) has been used and in which the positions of 10 fiducial GPS stations have been constrained. The precision of our positioning solutions obtained with Niell mapping function (1996) is millimetric, which is enough for our meteorological application. To obtain our MET observations, a secondary analysis is processed. Zenith delays and horizontal tropospheric gradients (two components, north-south and east-west) are calculated considering reference zenith and gradient variations of 0.02 $\mathrm{m\,h^{-1/2}}$ (Herring et al., 2010, Sect. 2.3). Tropospheric parameters of the ambiguity free solution have been adjusted with baselines greater than 2000 km. This is a way to decorrelate tropospheric measurements and vertical position estimations in the double difference process (Tregoning et al., 1998). For more details see Brenot et al. (2006).

Finally, ZTD measurements have been produced using a sliding window strategy with 6 sessions of 12 h of data shifted by 4 h for daily measurements (see Chapt. 1, Brenot 2006). A cut-off angle of 10° has been applied. ZTD and gradient observations have been assessed with a time resolution of 15 min.

3.2 Isotropic and anisotropic contributions of humidity by GNSS

ZTD represents the mean isotropic contribution of the neutral atmosphere mapped in the zenith direction using a mapping function (Niell, 1996). This means zenith contribution is obtained resolving ambiguities of the two phases of bi-frequencial GNSS signal (Bock et al., 1985; Leick, 1989) and considering a priori Zenith Hydrostatic Delays (ZHD) combined with Zenith Wet Delays (ZWD) adjustments established from slant delay variations recorded in the direction of each visible satellite (Tregoning and Herring, 2006); see Brenot et al. (2006) for a description of ZHD and ZWD.

ACPD
12, 20351–20382, 2012

Double difference of delays of the ionosphere-free combination (Brenot and Warnant, 2008) are used to assess ZTD (least-square adjustment). In addition horizontal gradients of delay are resolved to improve the slant delay reconstruction (Chen and Herring, 1997). GNSS gradients, described by two components NS and EW, estimate the mean local anisotropic contribution of slant path delay around a GNSS antenna; GAMIT normalised this contribution at 10° of elevation (centimetric values of NS and EW components). Contributions of GNSS gradients to slant delays (Chen and Herring, 1997) can be mapped in the zenith direction (Niell ,1996); millimetric values can be observed and will be used in this study. Figure 4 shows time series of ZTD and (NS, EW) gradient components for two Belgian GNSS stations (ERPE and NAMR), as well as the time series of radar precipitation. We can see that strong precipitation was observed during the 28–29 June 2005 event, which often coincided (63 %) with high variations of ZTD (increase or decrease of 8 mm) associated with high values of gradient components (amplitude 2 times over mean amplitude); see Fig. 1. Nevertheless we found a low Pearson correlation between radar precipitation and GNSS gradient amplitudes for all GNSS stations.

3.3 Improvement of humidity field by GNSS gradients

Using the Belgian dense network of GNSS stations (baselines from 5 to 30 km) and observations with a time resolution of 15 min, it is possible to characterise the humidity of the neutrosphere. The initiation of a convective system takes place for some cases in an area of few square kilometres, for this reason we have combined ZTD and gradients to improve the spatial resolution of our humidity field assessments. Our strategy is the following: considering the axis indicated by a gradient $\overrightarrow{G}$, two additional ZTD pseudo-observations have been considered (one wetter in the direction of the vector and an other one drier in the opposite direction). Our tests on the Belgian dense network (Neméghaire and Brenot, 2010) have shown that 10 km on either side of the GNSS site is the most relevant distance to detect small scale tropospheric structures of the troposphere (like a convective system of few kilometres). GNSS gradients (differential

ACPD
12, 20351–20382, 2012

values in the zenith direction) can be propagated horizontally by multiplying this contribution by the distance in kilometres (Walpersdorf et al., 2001). Then additional pseudo-observations of ZTD can be considered in our 2-D interpolated field with an adjustable tension continuous curvature surface gridding algorithm (Smith and Wessel, 1990). To avoid the signature of orography in ZTD measurements, we have applied an altitude correction (hydrostatic correction) to sea level as introduced by Saastamoinen (1972) and improved by Vedel et al. (2001). In Fig. 5, we can clearly see an improvement of the resolution of humidity field observed by GNSS.

The meteorological situation and the location of water vapour bubbles observed by GNSS are in a good agreement with radar precipitation. We can see in Fig. 1 that strong horizontal GNSS gradients are observed when significant hourly precipitation is recorded by meteorological radar from 12:00 to 16:00 UTC. This is evidence that the humidity field was characterised by a strong anisotropy during this period (see Fig. 5). The next step of our study is to implement H_2O alerts according to a specific configuration of the GNSS humidity field.

4 Implementation of H_2O alert by GNSS

A meticulous observation of ZTD and gradient time series has shown that for some regions a typical configuration can be observed before initiation of deep convection. This configuration is described by a significant local decrease of ZTD (drier region) following by a strong increase of ZTD (wetter region). This dry/wet contrast evolution is illustrated in Figs. 5b and 6 around 12:00 UTC for 4 stations of the Belgian dense network.

ZTD and gradients are estimated in the zenith direction considering all visible satellites. For a tropopause around 10 km of altitude and a cut-off angle of 10°, the radius of the tropospheric area considered by GNSS does not exceed 50 km. A gradient $\vec{G}$ with an amplitude of 0.01 m in the east direction means that the ZTD in the East direction is higher (for example about 0.01 m at 25 km). We can easily see in Fig. 6 what

ACPD
12, 20351–20382, 2012

are the ZTD values around Erpe (ERPE), Namur (NAMR), Geraardsbergen (GERA) and Buggenhout (BUGG) stations in the direction of a gradient, because ZTD and the gradient are plotted on the same scale.

Using improvement by horizontal GNSS gradients of 2-D fields of ZTD which are equivalent to the humidity field (Brenot et al., 2006), we have established a gridded map of GNSS alerts with a high resolution (pixels of 3 km × 3.5 km). The conditions to obtain a H_2O alert for a pixel at time T are the following: a ZTD-decrease of 0.008 m from T-30 min to T-15 min followed by a ZTD-increase of 0.015 m from T-15 min to T. H_2O alerts are shown by blue lines in Fig. 6. GNSS observations have been calculated every 15 min.

5 Indicators of deep convection

We have considered two external meteorological indicators of deep convection. The first one is based on reflectivity observations from a C-band weather radar located at Wideumont in the south of Belgium. The radar performs a 5-elevation scan every 5 min and a 10-elevation scan every 15 min. The latter is used to derive echo top values, which gives for a given threshold the maximum height where reflectivity values at least equal to this threshold are measured (Delobbe and Holleman, 2006). In this study we use a 38-dBZ threshold and we consider that a 38-dBZ echo top higher than 5 km represents a good indicator of deep convection.

During the rainfall event of the 29 June 2005, we can see that at 12:05 UTC radar echoes top indicate deep convection for 3 cells around Brussels (see Fig. 7). We have seen in Sect. 3.2 refering to Figs. 1 and 6 that a strong activity has been recorded by radar hourly precipitation and GNSS horizontal gradients. At the same time (Fig. 6 and 7) high values of the GNSS horizontal gradients point in direction of the convective cells where the maximum of humidity and convection occurred.

Figure 8 shows a vertical cut of radar reflectivity. GNSS gradient of the BUGG station points the local tropospheric anisotropy towards the convective cell located between

ACPD
12, 20351–20382, 2012

Brussels and Buggenhout. This convective cell had a vertical extension of more than 12 km. The least-square adjustment of GNSS gradients considers all the visible GNSS satellites; note that for the station of Brussels located close to several convective systems (see Fig. 8), no significant anisotropy is observed by the gradient. By contrast the GERA station observes a strong local anisotropy. We can see in Fig. 8 that all high values of the gradients point in the direction of cells identified by radar (see for example NAMR station).

The second indicator of deep convection that we use is infrared radiance from the SEVIRI instrument on METEOSAT Second Generation. If the effective radiance (channel 09) is less than 200 digital counts (DC) ($\approx 30.55\,\mathrm{W\,m^{-2}\,sr^{-1}\,cm^{-1}}$) we consider that deep convection took place.

Over Belgium, the SEVIRI resolution is about 3 km (E–W) × 5 km (N–S). The infrared 10.8 µm channel has been selected because the channel presents the best correlation with the cloud top height. In the weather office of most national meteorological services, this channel is usually used to detect and track convective systems. Humidity detected by GNSS gradients does not always point strictly in the direction of convective cells and clouds with the highest top identified by SEVIRI. Nevertheless high GNSS gradients always point in the direction of cloud with high top altitude and humidity detected by SEVIRI (Fig. 9). We find a good correspondence between low IR radiances and high gradient amplitudes; 65 % of GNSS sites with gradient amplitudes higher than 0.02 m show IR radiances under 220 DC ($\approx 34.65\,\mathrm{W\,m^{-2}\,sr^{-1}\,cm^{-1}}$) that is a sign of convection. A Pearson anti-correlation of 0.36 is obtained between IR radiance and horizontal GNSS gradient amplitudes.

6 First results of GNSS H_2O alert validation

To estimate the score of our H_2O GNSS alerts we consider that an alert is validated if an indicator of deep convection (by radar and/or by SEVIRI) is observed during the next 50 min. To validate our H_2O alert, the altitude of the 38 dBZ radar echo and the

ACPD
12, 20351–20382, 2012

SEVERI infrared radiance have been determined for the same grid. For this study, we have considered radar and SEVIRI observations every 15 min (at 05, 20, 35 and 50 min each hour). GNSS measurements and alerts are obtained every 15 min (at 00, 15, 30, 45 min).

The more active period of this event was between 11:00 and 16:00 UTC on the 29 June 2005. To show the application for nowcasting of our alert system, our improved ZTD 2-D fields, our GNSS H_2O alert 2-D fields, radar echoes top, and 2-D fields of SEVIRI radiances from 10:45 to 13:30 UTC are presented in Fig. 10. GNSS gradients are plotted on our interpolated ZTD fields (see Sect. 3.3). For H_2O alert, radar echoes top, and SEVIRI IR radiance fields, a grid of 3 km × 3.5 km (size of pixel) is used to obtain images. 12 times are shown in this figure (every 15 min). We will give a description of these times using all 2-D fields presented in Fig. 10.

Period a and b: No GNSS alert was observed at 10:45 and 11:00 UTC, but we noted that a strong decrease of humidity took place around NAMR station at 11:00 UTC. To the east of the NAMR region, a bubble of humidity was observed, which was initiated by a dry-wet dipole in this region.

Period c (11:15 UTC): There were 25 pixels with GNSS H_2O alerts around NAMR. We noted an increase of humidity on the north-west side of NAMR.

Period d (11:30 UTC): There were 24 pixels with H_2O alerts around ERPE (on the north and the south-east side). We observed an increase of humidity in this region. Humidity (associated with the formation of cloud over a deep vertical extent) coming from the north was confirmed by IR radiance from SEVIRI. Instability was shown by radar echoes top for this zone. A strong decrease of humidity was observed to the south of ERPE (dry-wet dipole).

Period e (11:45 UTC): There were 62 GNSS alerts around GERA (strong increase of humidity). We observed an increase of humidity for all stations located on the east side of the GERA-NAMR line. Convection started around NAMR.

ACPD
12, 20351–20382, 2012

Period f (12:00 UTC): GNSS gradients observed strong humidity to the south-east of ERPE. Strong precipitation and convection are shown by radar with a high vertical extension (see Fig. 8).

Period g (12:15 UTC): There were 6 GNSS alerts on the south side of ANTW, and 14 alerts on the east side of MOHA. A strong increase of humidity was observed around ANTW and MOHA stations. We can see evidence of a dry-wet dipole between BUGG and ANTW regions. BUGG station measured a strong GNSS gradient.

Period h (12:30 UTC): There were more than 80 alerts around BUGG which took place after a dry-wet contrast and a strong increase of humidity. There were also more than 80 alerts around ONHA station with an increase of humidity in this region. We noted a dry-wet dipole between OLLN and NAMR. Strong horizontal gradients of delay pointed in the direction of this wet area. Humidity and clouds are observed by SEVIRI around ANTW, MECH and BERT stations.

Period i (12:45 UTC): There were about 60 alerts around OLLN, with a dry-wet dipole between ONHA and MOHA stations. We observed strong humidity and gradients around MECH-BUGG and MOHA stations. Convection was detected by SEVIRI around GERA station.

Period j (13:00 UTC): There were about 50 alerts around OSTI with a strong increase of humidity in the triangle OSTI-NIKL-MECH. On the other hand, a dry patch was shown (ZTD field) around MECH station. A dry-wet dipole was observed between this patch and the wet triangle. About 50 alerts are generated around ONHA with an increase of humidity in this region. Convection was detected by echoes top radar around BERT, OLLN and MOHA stations. Convection was also detected by IR radiance around OSTI and GERA stations.

Period k (13:15 UTC): There were more than 70 alerts around MECH, with an increase of humidity to the east of this station. Wet regions detected by ZTD corresponded to regions with low IR radiances (convection identified by SEVIRI). More than 70 alerts took place around MOHA with an increase of humidity in this region. Strong

ACPD
12, 20351–20382, 2012

precipitation and convection are detected by radar around MOHA, OLLN and BUGG stations.

Period I (13:30 UTC): No alerts. At this time several cells with strong vertical extension are observed by the radar. Humidity, instability and clouds are detected on the south side of Belgium, as well as between ROOS and OSTI stations and on the north-east side of Belgium.

The analysis of Fig. 10 is a bit exhaustive, but there is considerable information for nowcasting. To summarise, the analysis of these periods shows that GNSS H_2O alerts are the result of dry-wet contrasts in time (strong increase and decrease) and dry/wet contrasts in space (dipole). That means a dry region is close to a wet region and there is a transfer of water vapour in this region. We observed strong amplitudes of gradients pointing towards wet areas with a strong instability. This shows the application of these observations for nowcasting. Statistical results and validation of our GNSS H_2O alerts generated, are shown in Table 1. We can see that 72 % of our alerts are validated by radar and SEVIRI (score of 39 % for radar and 56 % for SEVIRI) for this period.

The location of convection indications from radar and SEVIRI do not always correspond. Table 2 shows statistical results for the whole period under study. Using observations with a time-resolution of 15 min, we have interpolated linearly ZTD and gradient measurements for a time-resolution of 5 min. We can follow precisely the evolution of the humidity field and the application of our GNSS alerts for nowcasting. When no meteorological activity and deep convection is present, no alert was generated. Rain was recorded by rain gauges and radar on the 1 and 2 July (passage of a front of cloud system). No GNSS alert took place for these days. No dry/wet dipole and no strong contrast in time of humidity was observed by GNSS. We can see that the linear increase of ZTD and gradient time-resolution can improve our GNSS alert system. In fact, the number of alerts increased and in some cases, alerts took place earlier.

ACPD
12, 20351–20382, 2012

7 Conclusions

The aim of this paper was to see if preliminary signs of the initiation of deep convection can be established from post-processed meteorological GNSS observations (zenith total delay of the neutrosphere, called ZTD or commonly "tropospheric delay", and horizontal gradients of delay or commonly called "wet gradients"). Our study was focused on the rainfall event of the 28–29 June 2005 over Belgium. An overview of this meteorological event is presented. The time-resolution of our calculations of GNSS observations (from the 26 June to the 2 July 2005) used in this study is 15 min. The Belgian GNSS dense network (about 70 stations) has baselines from 5 to 30 km. The strategy used to measure our GNSS observations is presented.

Previous work by Walpersdorf et al. (2001) has shown the use of GNSS to describing the approach of a front towards Marseille in the south-east of France in 1998. Iwabuchi et al. (2003) have also shown that the temporal and spatial variations of GNSS gradients matched well with the moisture field determined by ZTD and with the meteorological condition in summer 1996 over the Japan Islands (in particular during the passage of a weather front). In our study we validate the application of GNSS for meteorology by comparison with synoptic observations, weather radar and SEVIRI instrument on METEOSAT satellite. We have shown that GNSS gradients with high amplitudes point in the direction of tropospheric wet structures identified by radar and SEVIRI (correspondence of 65 % between high values of each techniques). This paper shows how to use gradients to improve the resolution of ZTD and humidity fields by GNSS. Note that GNSS delay variations are driven by humidity variations and integrated water vapour (IWV). In this paper we prefer to use initial GNSS ZTD measurements rather than IWV conversion (Brenot et al., 2006). A meticulous observation of ZTD and gradient time series has shown that a typical configuration of humidity field can be observed before the initiation of deep convection. A dry-wet contrast in time (strong increase and decrease) and in space (dry/wet dipole formed by two regions a few kilometres distant) can take place a few ten of minutes before. This dry/wet contrast of GNSS ZTD field

ACPD
12, 20351–20382, 2012

allows us to establish H_2O alerts based on a substantial decrease of ZTD followed by a strong increase of ZTD. To validate our GNSS alert, we present two external meteorological indicators of deep convection. The first one uses C-band weather radar (5.64 GHz frequency) and echoes top measurements (reflectivities larger or equal to 38 dBZ at an altitude higher than 5 km), which represents a good indicator. The second one uses infrared radiance from the SEVIRI instrument on METEOSAT Second Generation. If effective radiance (channel 09) is less than 200 $W m^{-2}$ we consider that deep convection has taken place. To estimate the score of our H_2O alert by GNSS we consider that an alert is validated if an indicator of deep convection (by radar and/or by SEVIRI) takes place 50 min after this alert. Alerts and indicators are established for the same grid (pixel 3 km × 3.5 km). The score obtained is more than 80 % during the week of our case study. We can see that a linear increase of ZTD and gradient time-resolution can improve our GNSS alert system. In fact the number of alerts increased, and in some cases, alerts took place earlier.

Strong amplitudes of horizontal gradients point to wet areas with strong instability. These measurements represent a real opportunity for nowcasting. We have shown the key role of GNSS horizontal gradients in detecting water vapour bubbles and associated contrasts of humidity which are forerunners of deep convection. The rainfall event of 2005 is an unusual situation with the creation of a significant number of convective cells. We plan to test our alert for other weather situation.

Our study considers post-processed observations estimated with the final orbits of satelites provided by the International GNSS Service (http://igscb.jpl.nasa.gov). Our GNSS measurements have a high sensitivity to humidity in comparison to near real-time (NRT) observations. The next step of this study is to validate our alert with NRT ZTD measurements in the frame of EUMETNET GPS Water Vapour (EGVAP project, 2004–2008, 2009–2012), see Haan et al. (2006). Clearly the score can not be as good as with post-processed observations. NRT gradients clearly need to be considered. The use of improved mapping functions (Boehm and Shuh, 2004; Boehm et al., 2006a, 2006b) and the increase of positioning solutions (Tregoning and Watson, 2009, 2011)

ACPD
12, 20351–20382, 2012

show that the quality of NRT ZTD measurements is increasing as well as the time-delay (about 5 min after the observation times) to obtain NRT observations (Haan et al., 2009).

It is important to combine good quality ZTD and gradient observations (high sensitivity to humidity) with a time-delay less than 10 min after observation time (for operational use). We are considering using such a GNSS alert system in Belgium to support forecasters, as shown in Fig. 11. The quality of measurements depends on the precision of the positions of stations and meanly on the quality of orbits as well as on the number and the spatial distribution of stations. On the other hand, the time of calculations increases unlinearly with the number of stations. A good balance between the time of calcultations and the quality of measurements is required to generate NRT GNSS H_20 alerts. In addition to a good ratio of quality/time delivery of observations, improvement of such a service in NRT could also come from the combination of our alert with numerical weather prediction. More precise forecasts of locations of deep convection initiation could be expected with such an approach.

Acknowledgements. We would like to thank WALCORS, FLEPOS, EUREF IGS and René Warnant for providing the rinex data used in this paper. Thank you also to Bob King for the use of GAMIT software and to Paul Wessel for all the useful Generic Mapping Tools (GMT). Thank you also to Fabien Debal for his advice. We really appreciate and are grateful for all the comments and corrections that Geraint Vaughan, editor of this special issue of the Water Vapour in the Climate System (WAVACS) COST action, gave to us.

cost EUROPEAN COOPERATION IN SCIENCE AND TECHNOLOGY

This publication is supported by COST – www.cost.eu

References

Altamimi, Z., Sillard, P., and Boucher, C.: ITRF 2000: a new release of the international terrestrial reference frame for earth science applications, J. Geophys. Res., 107, 2214, doi:10.1029/2001JB000561, 2002.

ACPD

12, 20351–20382, 2012

Bevis, M., Businger, S., Herring, T. A., Rocken, C., Anthes, R. A., and Ware, R. H.: GPS meteorology: remote sensing of atmospheric water vapor using the global positioning system, J. Geophys. Res., 97, 15787–15801, doi:10.1029/92JD01517, 1992.

Bock, Y. R., Abbot, R. I., Counselman III, C. C., Gourevitch, S. A., and King, R. W.: Establishment of three-dimentional geodetic control via interferometry with global positioning system, J. Geophys. Res., 90, 7689–7703, doi:10.1029/JB090iB09p07689, 1985.

Boehm, J. and Schuh, H.: Vienna mapping functions in VLBI analyses, Geophys. Res. Lett., 31, L01603, doi:10.1029/2003GL018984, 2004.

Boehm, J., Niell, A. E., Tregoning, P., and Schuh, H.: Global mapping function (GMF): a new empirical mapping function based on numerical weather model data, Geophys. Res. Lett., 33, L07304, doi:10.1029/2005GL025546, 2006a.

Boehm, J., Werl, B., and Schuh, H.: Troposphere mapping functions for GPS and very long baseline interferometry from European Centre for Medium-Range Weather Forecasts operational analysis data, J. Geophys. Res., 111, B02406, doi:10.1029/2005JB003629, 2006b.

Brenot, H.: Potentiel de la mesure GPS sol pour l'étude des pluies intenses méditerranéennes, Ph.D. thesis, Université Joseph Fourier de Grenoble, Grenoble, France, 2006 (in French and English).

Brenot, H. and Warnant, R.: Characterization of the Tropospheric Small-Scale Activity, Technical Report ESA, WP250, GALOCAD project, 2008.

Brenot, H., Ducrocq, V., Walpersdorf, A., Champollion, C., and Caumont, O.: GPS zenith delay sensitivity evaluated from high-resolution numerical weather prediction simulations of the 8–9 September 2002 flash flood over southeastern France, J. Geophys. Res., 111, D15105, doi:10.1029/2004JD005726, 2006.

Chen, G. and Herring, T. A.: Effects of atmospheric azimuthal asymetry on the analysis of space geodetic data, Geophys. Res. Lett., 102, 20489–20502, doi:10.1029/97JB01739, 1997.

Delobbe, L. and Holleman, I.: Uncertainties in radar echo top heights used for hail detection, Meteor. Appl. (Royal Met. Society), 13, 361–374, 2006.

Gradinarsky, L. P.: Sensing Atmospheric Water Vapor Using Radio Waves, Ph.D. thesis, School of Electrical Engineering, CHALMERS University of Technology, Göteborg, Sweden, 2002.

Haan, S., Jones, J., and Vedel, H.: EUMETNET GPS Water Vapour (EGVAP), Presentation at European Meteorological Society, Ljubljana, Slovenia, 2006.

ACPD
12, 20351–20382, 2012

Haan, S., Holleman, I., and Holtslag, A. A. M.: Real-time water vapor maps from a GPS surface network: construction, validation, and applications, J. Appl. Meteor., 45, 467–475, doi:10.1175/JAM2338.1, 2009.
Herring, T. A., Davis, J. L., and Shapiro, I. I.: Geodesy by radio interferometry: the application of Kalman filtering to the analysis of very long baseline interferometry data, J. Geophys. Res., 95, 12561–12581, doi:10.1029/JB095iB08p12561, 1990.
Herring, T. A., King, R. W., and McClusky, S. C.: Documentation for the GAMIT GPS Analysis Software, version 10.4, Tech. rep., Mass. Inst. Tech., Cambridge, USA, 2010.
Iwabuchi, T., Miyazaki, S., Heki, K., Naito, I., and Hatanaka, Y.: An impact of estimating tropospheric delay gradients on tropospheric delay estimations in the summer using the Japanese nationwide GPS array, J. Geophys. Res., 108, 4315, doi:10.1029/2002JD002214, 2003.
Leick, A.: GPS Satellite Surveying, Wiley-Interscience, New York: Wiley, USA, 1989.
Neméghaire, J. and Brenot, H.: Etude du potentiel d'utilisation des observations GNSS pour l'analyse météorologique et la prévision à très court terme, Publication scientifique de l'Institut Royal Météorologique de Belgique, Brussels, Belgium, October 2010 (in French).
Niell, A.: Global mapping functions for the atmosphere delay at radio wavelengths, J. Geophys. Res., 101, 3227–3246, 1996.
Saastamoinen, J.: Atmospheric Correction for the Troposphere and Stratosphere in Radio ranging of satellites, in: The Use of Artificial Satellites for Geodesy, edited by: Henriksen, S. W., Mancini, A., and Chovitz, B. H., Geophys. Monogr. Ser., 15, 247–251, 1972.
Smith, W. H. F. and Wessel, P.: Gridding with continuous curvature splines in tension, Geophysics, 55, 293–305, doi:10.1190/1.1442837, 1990.
Tregoning, P. and Herring, T. A.: Impact of a priori zenith hydrostatic delay errors on GPS estimates of station heights and zenith total delays, Geophys. Res. Lett., L23303, 33, doi:10.1029/2006GL027706, 2006.
Tregoning, P. and Watson, C.: Atmospheric effects and spurious signals in GPS analyses, J. Geophys. Res., 114, B09403, doi:10.1029/2009JB006344, 2009.
Tregoning, P., Boers, R., O'Brien, D., and Hendy, M.: Accuracy of absolute precipitable water vapor estimates from GPS observations, J. Geophys. Res., 103, 28701–28710, doi:10.1029/98JD02516, 1998.
Vedel, H., Mogensen, K., and Huang, X.-Y.: Calculation of zenith delays from meteorological data comparison of NWP model, radiosonde and GPS delays, Phys. Chem. Earth, 26, 497–502, 2001.

ACPD
12, 20351–20382, 2012

Walpersdorf, A., Calais, E., Haase, J., Eymard, L., Desbois, M., and Vedel, H.: Atmospheric gradients estimated by GPS compared to a high resolution numerical weather prediction (NWP) model, Phys. Chem. Earth, 26, 147–152, 2001.

ACPD

12, 20351–20382, 2012

Table 1. Statistics results between 10:45 and 12:00 UTC the 29 June 2005. For each H_2O alert (pixel), if deep convection is indicated by radar and/or SEVIRI, one count is obtained. Final scores are set with a normalisation in percentage.

Periods	Number of H_2O alert	Score (radar)	Score (SEVIRI)	Final Score
29 Jun 2005 10H45	0	–	–	–
29 Jun 2005 11H00	0	–	–	–
29 Jun 2005 11H15	32	50.0 %	9.4 %	53.1 %
29 Jun 2005 11H30	24	62.5 %	0.0 %	62.5 %
29 Jun 2005 11H45	63	52.4 %	57.1 %	62.0 %
29 Jun 2005 12H00	6	100.0 %	83.3 %	100.0 %
29 Jun 2005 12H15	21	52.4 %	33.3 %	85.7 %
29 Jun 2005 12H30	181	19.4 %	43.6 %	50.3 %
29 Jun 2005 12H45	80	76.3 %	45.0 %	91.3 %
29 Jun 2005 13H00	115	32.17 %	94.8 %	95.7 %
29 Jun 2005 13H15	167	33.1 %	67.0 %	76.8 %
29 Jun 2005 13H30	0	–	–	–
all this period	689 %	39.1 %	56.1 %	72.2 %

ACPD
12, 20351–20382, 2012

Table 2. Number and score of our H_2O alert (GNSS observations from 26 June 2005 to 2 July 2005). Time resolution of GNSS observations is 15 min. In brackets are shown results when GNSS observations are interpolated linearly every 5 min.

Periods	Number of H_2O alert	Score (radar)	Score (SEVIRI)	Final Score
26 Jun 2005	0 (0)	–	–	–
27 Jun 2005	0 (0)	–	–	–
28 Jun 2005	798 (1853)	34 % (31 %)	70 % (71 %)	78 % (75 %)
29 Jun 2005	2821 (6384)	48 % (44 %)	82 % (84 %)	89 % (87 %)
30 Jun 2005	0 (0)	–	–	–
01 Jul 2005	0 (0)	–	–	–
02 Jul 2005	0 (0)	–	–	–
All days	3619 (8237)	45 % (41 %)	79 % (81 %)	86 % (84 %)

ACPD
12, 20351–20382, 2012

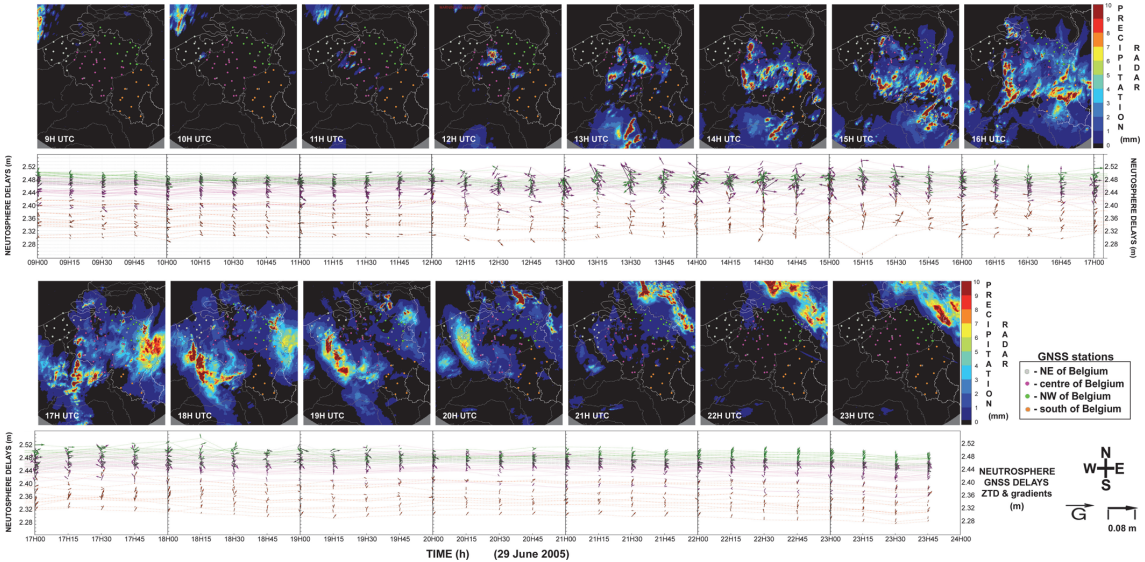

Fig. 1. Sequence of hourly precipitation detected by radar from 09:00 to 24:00 UTC (29 June 2005). GNSS stations are plotted on this map with 4 different colours dedicated to 4 geographical regions. Time series of GNSS horizontal gradients $\vec{G}$ are shown under using the same 4 dedicated colours.

ACPD
12, 20351–20382, 2012

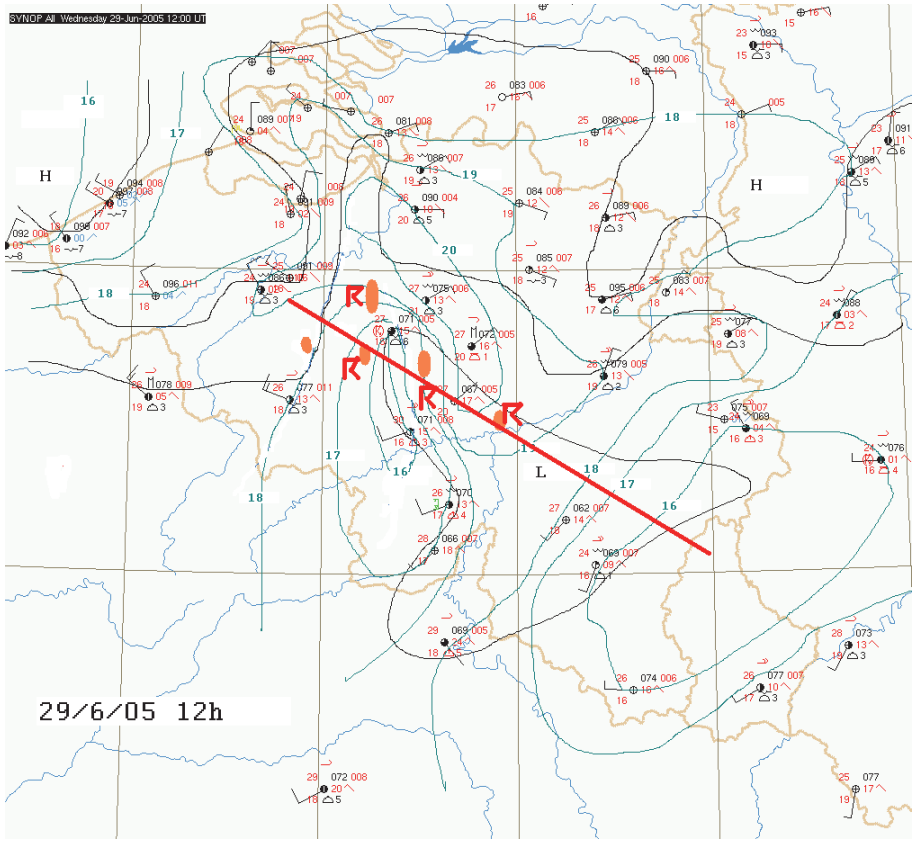

Fig. 2. Meso-scale surface analysis. Plot of a line of convergence is shown in red, radar precipitation in orange, and R symbol for rainfall event thunderstorms detected by SAFIR.

ACPD
12, 20351–20382, 2012

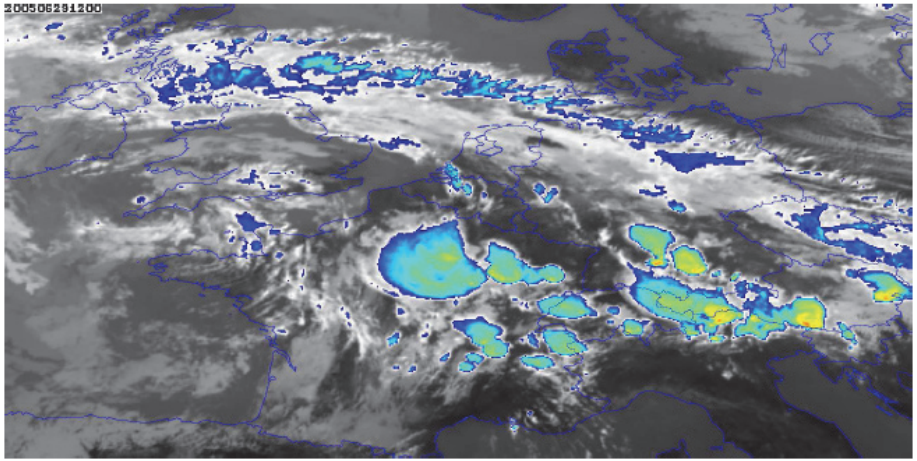

Fig. 3. SEVIRI image (IR channel) the 29 June 2005 at 12:00 UTC. Tops of coldest clouds are shown by colour patterns scaled from blue, orange to red according to decreasing temperature.

ACPD
12, 20351–20382, 2012

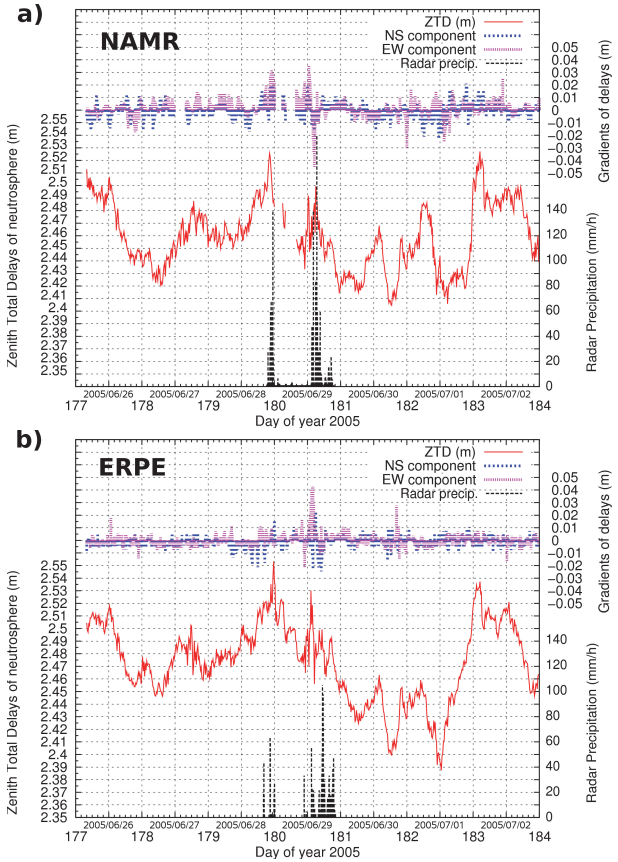

Fig. 4. Time series of GNSS Zenith Total Delays of neutrosphere (ZTD), GNSS horizontal gradients of delay (NS and EW components), and radar precipitation for **(a)** NAMR station (missing data the morning of the 29) and **(b)** ERPE station, from 25 June 2005 to 3 July 2005.

ACPD
12, 20351–20382, 2012

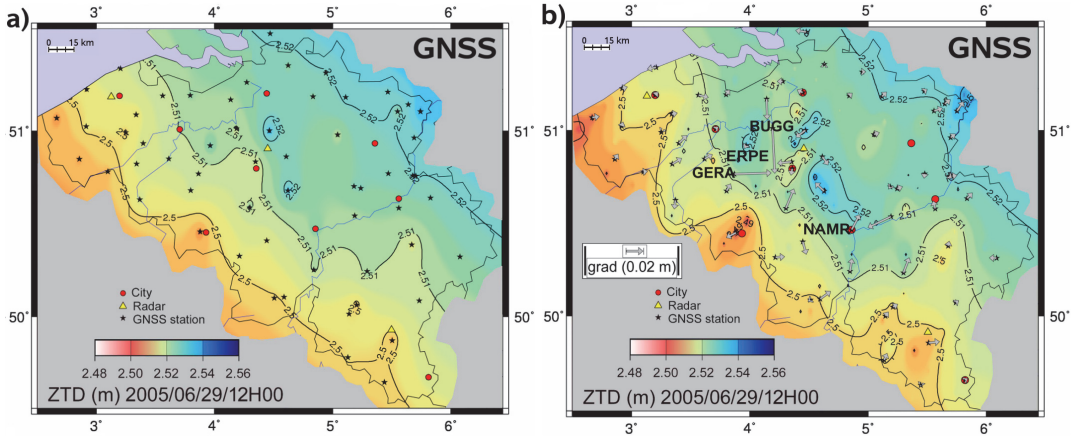

Fig. 5. (a) imaging of the 2-D field of ZTD with a classic interpolation (stations are plotted by black stars); **(b)** improvement of this field by GNSS gradients. These gradients $\vec{G}$ are plotted by grey arrows at each GNSS site. BUGG, ERPE, GERA and NAMR stations are plotted. Locations of 9 major cities (red circles) and meteorological radars (yellow triangles) are also plotted on these 2-D maps.

ACPD
12, 20351–20382, 2012

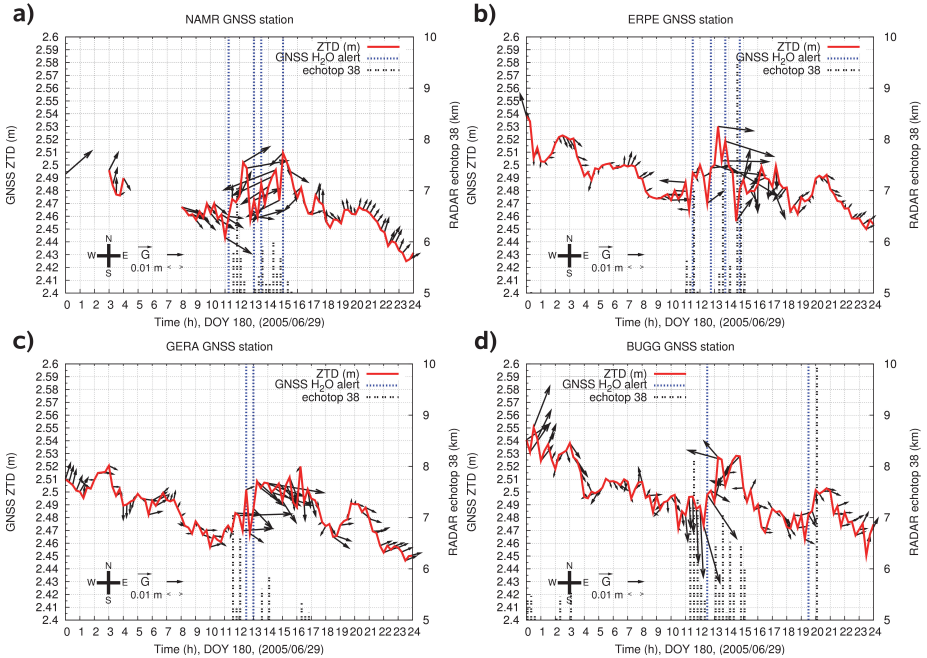

Fig. 6. Time series of ZTD and gradients **(a)** for NAMR, **(b)** ERPE, **(c)** GERA, and **(d)** BUGG stations (29 June 2005). GNSS H_2O alerts are shown by blue dotted lines. Altitudes of the highest 38 dBZ radar echoes are plotted for values over 5 km (black dash line).

ACPD
12, 20351–20382, 2012

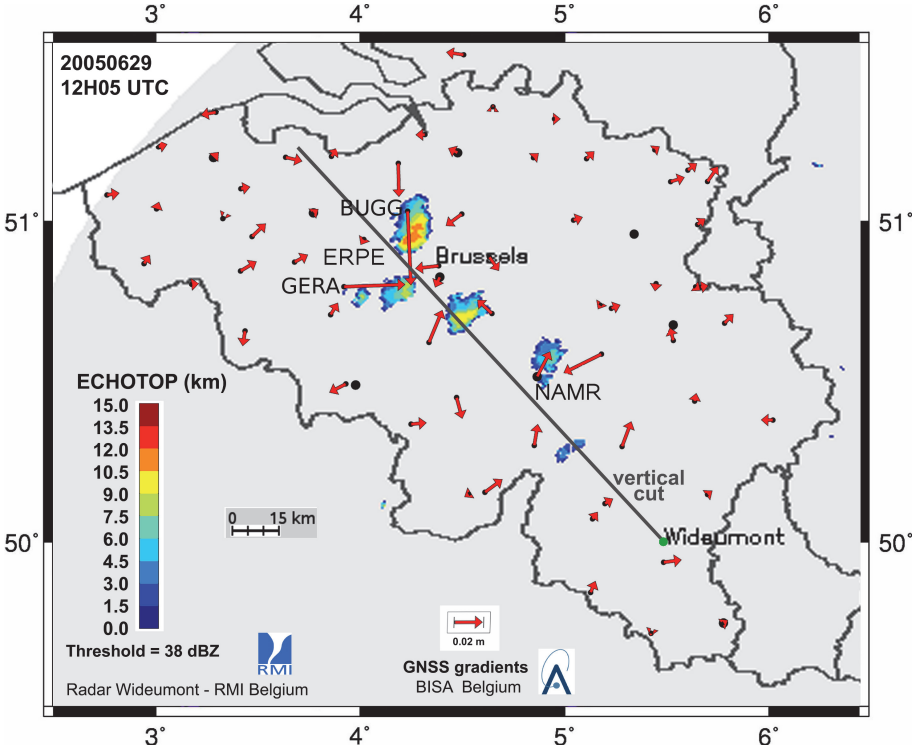

Fig. 7. Altitude of the highest 38 dBZ radar echo on the 29 June 2005 at 12:05 UTC. The black line shows the location of the vertical cut of radar reflectivity presented in Fig. 8. GNSS gradients are plotted with red arrows on stations (small black circles). The main Belgium cities are shown by big black circles and the Wideumont weather radar with a green circle.

ACPD
12, 20351–20382, 2012

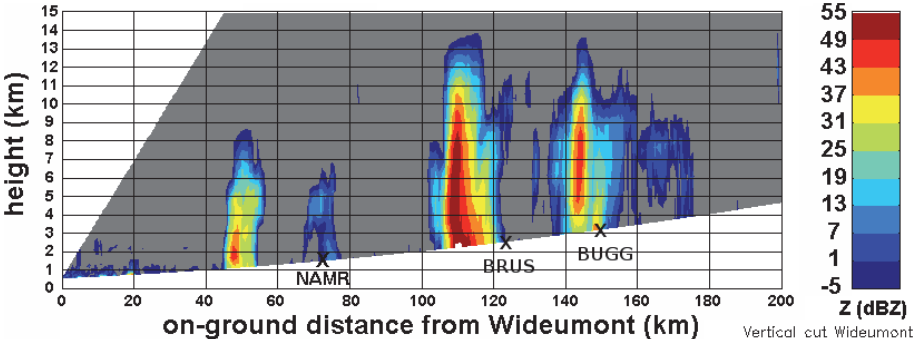

Fig. 8. Radar imaging of a vertical cut of reflectivy (in dBZ up to 15 km) from Wideumont radar to a distance of 200 km in the north-west direction (12:05 UTC, 29 June 2005). Projections of the BRUS and BUGG stations (respectively 6 km and 13 km distant) on this axis are plotted on this graph.

ACPD
12, 20351–20382, 2012

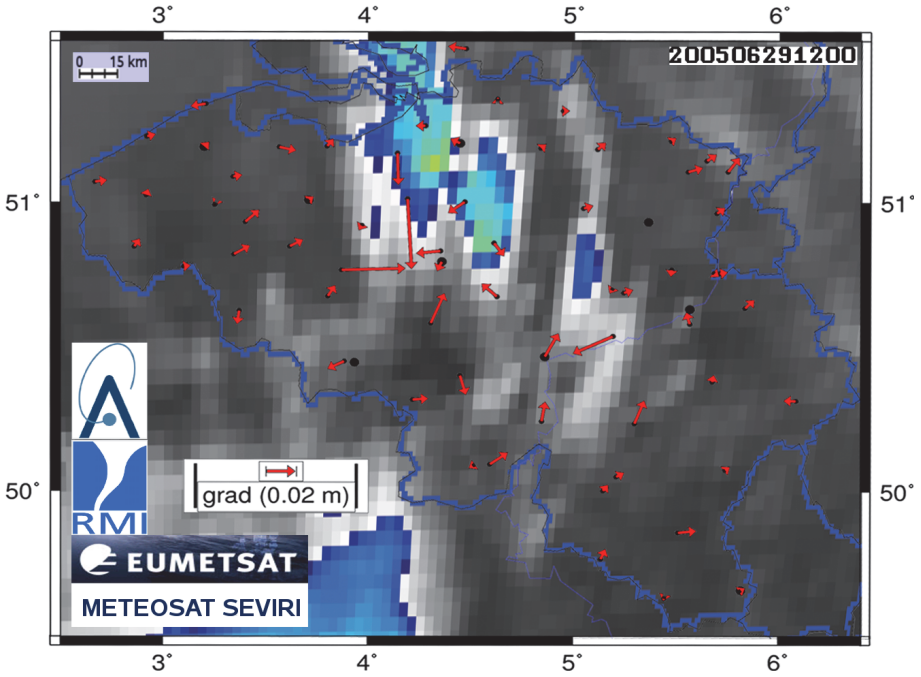

Fig. 9. Infrared radiance of the 10.8-μm channel of SEVIRI expressed in digital counts (DC) and GNSS gradients plotted with red arrows on stations (black small circles) at 12:05 UTC (29 June 2005). DC over 200 are scaled in white and grey for high values. DC under 200, where the convection takes place, are from blue to green and yellow for low values.

ACPD
12, 20351–20382, 2012

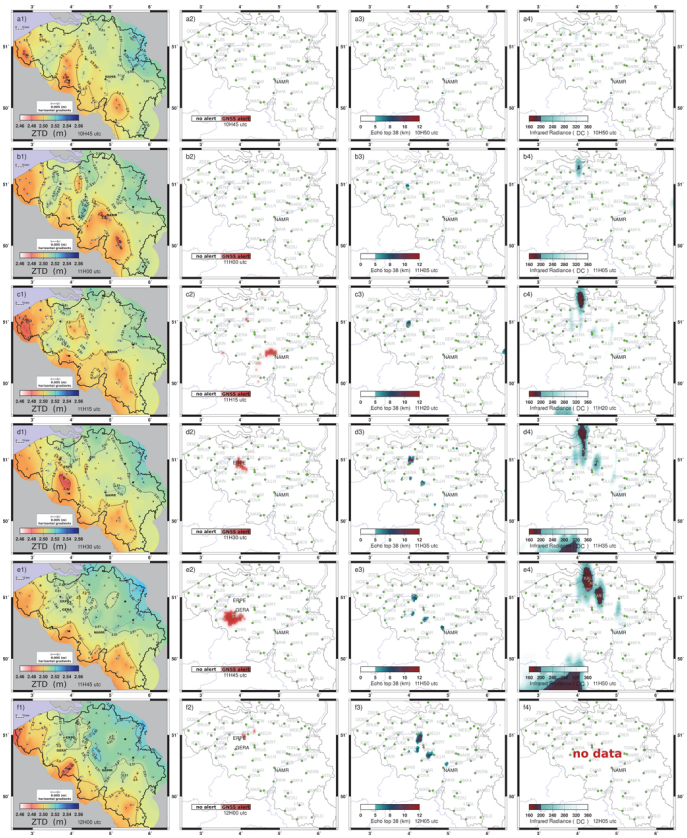

Fig. 10. 2-D fields of ZTD and horizontal gradients (in m) on the left column, followed by GNSS H_2O alerts (0 or 1), and by altitudes of the highest 38 dBZ radar echo (in km). The right column shows infrared radiances from SEVIRI in digital counts (DC). There is a time delay of 15 min between each 12 lines (GNSS fields start at 10:45 a.m.; echo top radar and SEVIRI radiance start at 10:50 UTC on the 29 June 2005).

ACPD
12, 20351–20382, 2012

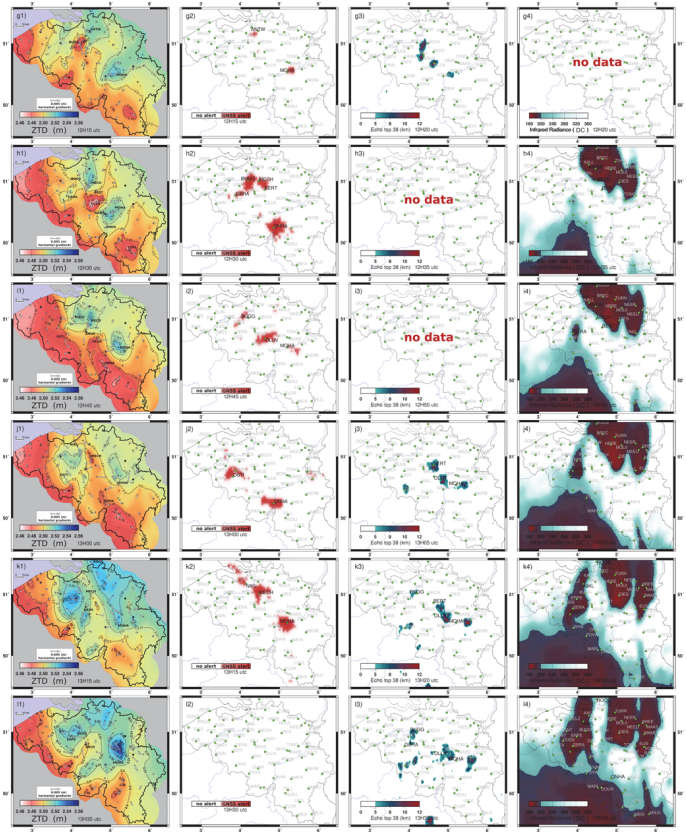

Fig. 10. Continued.

ACPD
12, 20351–20382, 2012

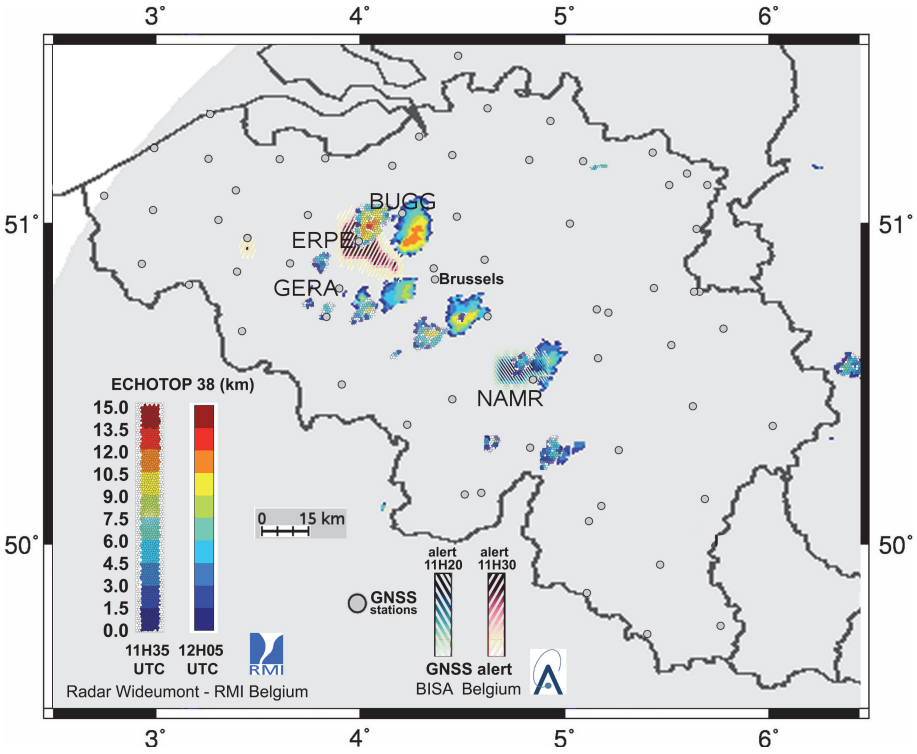

Fig. 11. GNSS H_2O alert (11:20 and 11:30 UTC) and radar echoes top (altitude of the highest 38 dBZ radar echo) at 11:35 and 12:05 UTC, the 29 June 2005.

ACPD
12, 20351–20382, 2012